



Article

Investigation of Welding Parameters of Dissimilar Weld of SS316 and ASTM A36 Joint Using a Grey-Based Taguchi Optimization Approach

Diah Kusuma Pratiwi ¹, Amir Arifin ^{1,*} , Gunawan ¹ , Alim Mardhi ² and Afriansyah ¹

¹ Department of Mechanical Engineering, Universitas Sriwijaya, Indralaya 30662, Sumatera Selatan, Indonesia

² Research Centre for Nuclear Reactor Technology, National Research and Innovation Agency, Tangerang Selatan 15314, Banten, Indonesia

* Correspondence: amir@unsri.ac.id

Abstract: A grey-based Taguchi method was applied to investigate the optimal operating conditions in shielded metal arc welding (SMAW) to join SS316 and ASTM A36. This work aims to set optimal parameters for the mechanical properties of the weld joint. The effects of various welding factors on electrode type, welding current, arc welding, and welding speed have to be characterized and optimized to achieve an optimum condition. An L9 orthogonal array was used to group the various components. The mechanical properties of a dissimilar weld joints were described through hardness, tensile and flexural strength tests. The optimum welding parameters were obtained simultaneously as an electrode type E309, a welding current of 100 A, an arc voltage of 14 V, and a welding speed of 4 cm/min, which predicted improve 23.0% in its performance.

Keywords: dissimilar weld; SMAW; SS315; low-carbon steel; Taguchi method; grey relational analysis (GRA); ANOVA



Citation: Pratiwi, D.K.; Arifin, A.; Gunawan; Mardhi, A.; Afriansyah Investigation of Welding Parameters of Dissimilar Weld of SS316 and ASTM A36 Joint Using a Grey-Based Taguchi Optimization Approach. *J. Manuf. Mater. Process.* **2023**, *7*, 39. <https://doi.org/10.3390/jmmp7010039>

Academic Editors: Dariusz Fydrzych, Jacek Tomków, Aleksandra Świerczyńska, Grzegorz Rogalski, Sergey G. Parshin, Chandan Pandey, Michał Landowski, Hamed Aghajani Derazkola and Thomas Hassel

Received: 17 December 2022

Revised: 26 January 2023

Accepted: 27 January 2023

Published: 2 February 2023



Copyright: © 2023 by the authors. Licensee MDPI, Basel, Switzerland. This article is an open access article distributed under the terms and conditions of the Creative Commons Attribution (CC BY) license (<https://creativecommons.org/licenses/by/4.0/>).

1. Introduction

The welding procedure has been applied to almost all industries since it was first discovered in 1800. Welding is a manufacturing process whereby two or more metal parts are bonded through heat, pressure and both forming a joint [1]. Commonly, the welding process is used in many industries and constructions, such as railroads, bridges, shipping, steel structures, and the automotive and maritime industries. Based on the joining process, welding can be classified into shielded metal arc welding (SMAW), submerged arc welding (SAW), gas metal arc welding (GMAW), gas tungsten arc welding (GTAW), and others. Welding based on the welded material can be divided into similar and dissimilar welding [2].

Commonly, in the industry, for engineering and cost reduction reasons, dissimilar metal welding is unavoidable. Dissimilar metal welding can be found widely in many production lines, such as boilers, rig towers, automotive components, and nuclear power plant component manufacturing. Dissimilar metal welding combines two types of materials with different contents, for example, welding between stainless steel and carbon steel or between duplex and carbon steel [3].

Much effort has been conducted in dissimilar welding research on weld metal composition, the influence of usage conditions, mechanical properties, and physical properties, and resistance to corrosion or oxidation. Some material pairs for dissimilar welding applications include martensite–austenite, duplex–carbon steel, austenite steel–inconel, and austenite–ferritic steel [4–6].

Some issues are still challenging in dissimilar metal welding, such as the difference in melting point temperature, brittle phase formation and solubility of the two metals, and residual stress due to differences in thermal conductivity and expansion coefficients [7–9].

Moreover, choosing a suitable filler wire is more challenging. Both the base materials and the filler material should be compatible. Hot cracking in the fusion zone and heat affected zone (HAZ) along with the formation of undesirable secondary phases in the weldment are the outcomes of inappropriate filler wire selection [10]. Mechanical-metallurgical characteristics and bead quality greatly influence the quality of a dissimilar weld joint.

Furthermore, welding parameters such as current, voltage, position, speed, and many more in the welding process have an essential role in determining weld joint quality [11,12]. Previous authors have utilized the shielded metal arc welding (SMAW) method for dissimilar joint metals. SMAW with a welding current of 150 A and an arc voltage in the range of 13 to 15 V was utilized by Manikandan et al. (2017) to create a joint between nickel-based superalloy Incoloy 800 and stainless steel AISI 316L [13]. Verma et al. (2016) have successfully joined 316L ASS and 22% Cr DSS 2205 with welding parameters of 70–120 A and 16–25 V for current and arc voltage, respectively [14]. Moreover, another study was performed by Verma et al. (2016), with a welding current of 120 A, a welding speed of 3.1–3.3 mm/s, and an arc voltage in the range of 25–26 V for joining A2205 and SS316L [15].

Optimizing dissimilar welding becomes challenging because of the many factors involved in the welding process, both controllable and uncontrollable. Ghosh et al. (2017) reported the effect of welding parameters GMAW on the mechanical properties of AISI 409 and AISI 316L through the Taguchi approach [16]. Daniyan et al. (2018) analyzed welding parameters to obtain predictive weld distortion and hardness models using the Taguchi method and response surface methodology (RSM) [17]. Mahmood and Alwan (2019) also utilized the Taguchi method approach to discuss the welding parameters' effect on steel's hardness and flexural strength, and to obtain the optimized values [18].

Stainless steels with austenitic compositions, such as SS316 and ASTM A36, are extensively utilized. SS316 is frequently used in industrial applications such as heat exchangers, dyeing equipment, and pipelines due to its corrosion resistance, high-temperature resistance, and mechanical properties. ASTM A36 generates welded and bolted metal structures for general construction and mechanical engineering applications. It has good machinability and ductility but is not corrosion resistant. Although many welded members fail because of tensile and bending failures, inappropriate hardness and poor tensile and bending strength may also cause failure. Many studies also do not consider welding parameters' effect on hardness, tensile, and bending strength.

This research investigates the effect of SMAW welding parameters (electrode type, welding current, arc voltage, and welding speed) on the hardness, flexural strength, and bending strength of SS316 and low-carbon steel to obtain optimized values.

2. Materials and Methods

In this work, SS316 and ASTM A36 have been taken as the raw material. The chemical composition of base materials is shown in Table 1, characterized by using metal analyzer Model PMI-Master Smart-Mobile optical emission spectrometers.

Table 1. Chemical composition of SS316 and ASTM A36 (Unit: %).

	Fe	C	Si	Mn	Cr	Mo	Ni	Al	Co	Cu	Nb
A36	98	0.18	0.24	0.87	0.22	0.01	0.013	0.02	0.004	0.016	0.018
SS316	67.6	0.046	0.645	0.908	18	2.12	10.1	0.003	0.24	0.129	0.014

Table 1 shows that SS316 consists of chromium 18%, molybdenum 2.12%, and nickel 10.1%. The chromium content encourages passivation, while molybdenum and nickel enhance stainless steel's corrosion, heat, and creep resistance. Commonly, austenitic stainless steel contains at least 8% nickel; however, the high-nickel alloy is required under a corrosive environment and high-temperature application.

The shielded metal arc welding was performed using a welding machine (Vantage 500 Deutz) with 30–575 A and 2.5–8 mm for the current and electrode ranges. The plate steel

of size 150 mm × 100 mm × 5 mm was machined with a V-groove with a 55° inclined angle for tensile and hardness testing. All welded specimens have passed a visual examination and an X-ray radiographic test. Following visual inspections and X-ray radiographic screening, the machining process is carried out to obtain a tensile test specimen.

A Hung Ta Type HT 9502 universal testing machine was utilized to investigate tensile strength and flexural strength based on the ASTM E8-08 standard of tension testing. The hardness value on the fusion zone was analyzed based on the ASTM E10-17 standard test method for Brinell hardness using BH-3CF Type from Tokyo Testing Machine MFG Co. Ltd., Japan,. Furthermore, a measuring microscope STM6 from Olympus was used to study the microstructural of the welding joints.

The Taguchi method is based on an orthogonal array experiment, which is a matrix of some rows and columns [19]. Each column represents certain factors or conditions that can change from one experiment to another. The arrays are called orthogonal because each level of each factor is balanced and can be separated from the influence of other factors in the experiment. The degrees of freedom are determined based on the main factors observed and the interactions observed, the number of levels of the factors observed, and the resolution of the desired experiment.

The Taguchi method offers an effective and efficient approach to improving quality design and performance. Moreover, the large number of experiments can be reduced by using Taguchi. An orthogonal array in the Taguchi method is used to investigate the interaction of entire process parameters. Taguchi’s procedure uses the *S/N* ratio to improve the performance characteristics. Typically, the *S/N* ratio can be characterized into three categories: the lower-the-better (Equation (1)), the larger-the-better (Equation (2)), and the nominal the-better (Equation (3)).

$$\frac{S}{N} = -10 \text{ Log} \left(\frac{1}{n} \sum Y^2 \right) \tag{1}$$

$$\frac{S}{N} = -10 \text{ Log} \left(\frac{1}{n} \sum \frac{1}{Y^2} \right) \tag{2}$$

$$\frac{S}{N} = -10 \text{ Log} \left(\frac{1}{n} \sum \frac{Y^2}{\sigma^2} \right) \tag{3}$$

where *Y* is the measured value of the response variable, *n* is the repeated experiment number, and σ is the standard deviation. The larger-the-better quality characteristic is employed to improve the tensile strength of weld joints through optimum process parameters in shielded metal arc welding. Furthermore, the confirmation experiment is conducted to confirm the optimal process parameters level [20,21].

Four welding parameters were designated, comprising electrode type, welding current, arc voltage, and welding speed, as shown in Table 2. The parameters were chosen based on common practical welding parameters and available equipment setting. An electrode with a diameter of 2.6 mm was used during welding and uses two layers. Furthermore, the experimental layout and factors distribution of the orthogonal array (L9) can be seen in Table 3.

Table 2. Factors and levels for the welding process.

Parameters	Level 1	Level 2	Level 3
Electrode type (A)	E308	E309	E312
Welding current (B)	90	100	110
Arc voltage (C)	14	16	18
Welding speed (D)	4	5	6

Table 3. Experimental layout and factor distribution of the orthogonal array (L9).

ExpNo	Factor				Experimental Welding Values			
	A	B	C	D	Electrode	Current (A)	Voltage (V)	Speed (cm/min)
1	1	1	1	1	E 308	90	14	4
2	1	2	2	2	E 308	100	16	5
3	1	3	3	3	E 308	110	18	6
4	2	1	2	3	E 309	90	16	6
5	2	2	3	1	E 309	100	18	4
6	2	3	1	2	E 309	110	14	5
7	3	1	3	2	E 312	90	18	5
8	3	2	1	3	E 312	100	14	6
9	3	3	2	1	E 312	110	16	4

The multiple responses in this study also are analyzed using a grey relational analysis (GRA). The grey relational analysis was devised to address problems associated with multiple choices, ambiguity, and discrete information [22]. As a result of this calculation, a single numerical score represents an average of several different responses. In GRA, the factor’s function is often ignored when the standardized value and reference sequence range are both very high. Furthermore, if the intent and direction of the components conflict, the GRA results may be erroneous. For this reason, before analysis, data pre-processing is performed to normalize the original reference sequence to a comparable sequence in the range of zero to one [23].

Grey relational generation is the phrase used to describe the process of pre-processing data via normalizing and converting it into a collection of sequences. When performing a pre-processing step with GRA, the response of the modified sequences can be divided into two quality characteristics, which are larger-the-better and smaller-the-better, respectively. Equation (4) can be used to normalize a sequence when the larger-the-better characteristic is present.

$$x_i^*(k) = \frac{y_i(k) - \min y_i(k)}{\max y_i(k) - \min y_i(k)} \tag{4}$$

where $x_i^*(k)$ is the sequence after pre-processing for the i th experiment, and $y_i(k)$ is the sequence of the mean responses for the i th experiment.

It is necessary to normalize the sequence before proceeding to the next stage, which is to calculate the deviation sequence of the reference sequence using Equation (5). Once the sequence has been normalized, the following steps must be completed:

$$\Delta_{0i}(k) = |x_0^*(k) - x_i^*(k)| \tag{5}$$

where deviation, reference, and comparability sequences are denoted by $\Delta_{0i}(k)$, $x_0^*(k)$ and $x_i^*(k)$. Equation (6) is then used to calculate the grey relational coefficient (GRC).

$$\xi_i(k) = \frac{\Delta_{min} + \zeta \Delta_{max}}{\Delta_{0i}(k) + \zeta \Delta_{max}} \tag{6}$$

where $\xi_i(k)$ is the GRC of individual response variables and is derived as a function of the minimum (Δ_{min}) and maximum (Δ_{max}) variances of each response. It is common practice to set the distinguishing or identification coefficient, denoted by the symbol ζ and specified in the range [0, 1], at 0.5 to provide equal weights to each parameter in the model. A composite grey relational grade (GRG) is then calculated by averaging the grey relational coefficient (GRC) of each response variable, as indicated in Equation (7).

$$\gamma_i = \frac{1}{n} \sum_{i=1}^n \xi_i(k) \tag{7}$$

where i is the value of GRG determined for the i th experiment, and n indicates the total number of performance characteristics measured across all experiments.

Analysis of variance (ANOVA) is utilized for both Taguchi and GRA as it allows quantitative evaluation of each factor's contribution to all response measurements. The purpose of the used analysis of variance is to discover the contribution of the components to the parameter design to determine the model's accuracy. For ANOVA, the total number of squares, the number of squares to the mean, the sum of the factor squares, and the sum of the error squares must be calculated.

3. Results and Discussion

Figure 1 shows the weld joint of SS316 and ASTM A36 with nine welding parameters referred to as the L9 orthogonal array. All the weld joints have been approved by radiographic examination, proving the soundness of the weld.



Figure 1. Weld joint appearance of SS316 (grey) and ASTM A36 (brownish).

Specimen parts that do not pass the screening will not be used to produce specimens. Incomplete penetration is the common defect that appears during the experiment. It occurs when the groove of the metal is not filled. Another fault, incomplete fusion, was observed in experiment No. 4. Incomplete fusion defects occur when there is a lack of proper fusion between the base metal and the weld metal. They can also appear between adjoining weld beads, creating a gap in the joint not filled with molten metal. Many factors contribute to defects during welding, including improper welding input parameters such as current, nasty filler metal and base metal, faster arc travel speed, the presence of oxides, scale, etc.

X-ray radiographic tests have been conducted for all nine samples. A few examples of typical copies of radiography film are given in Figure 2.

Table 4 shows all design experiments' hardness, tensile strength, and flexural strength. It is shown that the maximum hardness (275 HBW) is at E312, 110 A, 16 V, and 4 cm/min, the maximum tensile strength (433 MPa) is at E309, 100 A, 18 V, and 4 cm/min, and the maximum flexural strength (657 MPa) is at E308, 90 A, 14 V and 4 cm/min.

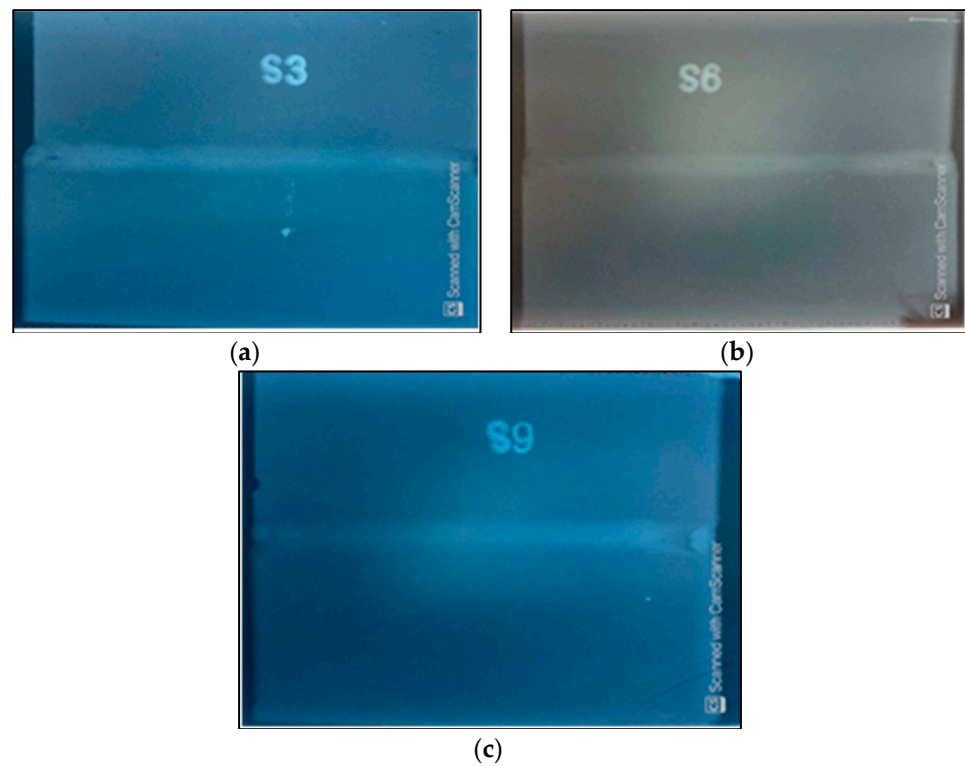


Figure 2. X-ray radiographic results of (a) experiment No. 3, (b) experiment No. 6 and (c) experiment No. 9.

Table 4. Orthogonal array (L9) experimental results.

No.	Factors				Response Values (Average)		
	A	B	C	D	Hardness (HBW)	Tensile Strength (MPa)	Flexural Strength (MPa)
1	E 308	90	14	4	215	430	657
2	E 308	100	16	5	212	416	641
3	E 308	110	18	6	206	370	558
4	E 309	90	16	6	212	370	630
5	E 309	100	18	4	267	433	573
6	E 309	110	14	5	261	412	616
7	E 312	90	18	5	253	413	490
8	E 312	100	14	6	259	406	482
9	E 312	110	16	4	275	391	383

3.1. Hardness Results

Hardness measurements were carried out on the fusion zone of the weld using the Brinell method. The study of four parameters (electrode type, welding current, arc voltage, and welding speed) for hardness, in terms of the main effects plot for means and the main effects plot for S/N ratios for each interaction, is shown in Figure 3. The highest yield of hardness signal to noise (S/N) ratio, based on larger-the-better, could be attained at the combined settings of A3, B3, C1, and D1, i.e., an electrode type of E 312, a welding current of 110 A, an arc voltage of 14 V and a welding speed of 4 cm/min.

Figure 3 shows that electrode type and welding current are essential in influencing hardness increase. The hardness decreased with increasing welding speed, and minimum hardness was obtained at 16 volts of arc voltage.

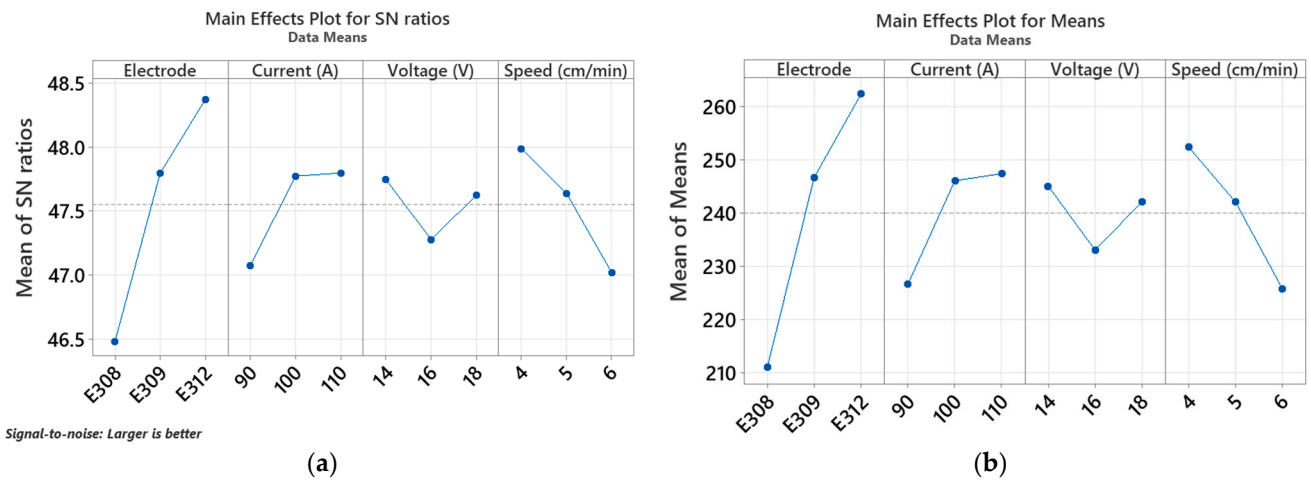


Figure 3. (a) S/N ratio and (b) mean response graphs for hardness.

The hardness of metal joints is affected by the concentration of alloys, which is related to carbon equivalent. It is usually used as a reference to determine steel metal joints' susceptibility to cold cracking. The presence of elements such as Cr, Mo, Ni, and Mn plays a vital role in forming phases that affect mechanical properties [24]. The Schaeffler diagram can predict phase formation in the fusion zone based on the dilution ratio of both materials [25]. The maximum hardness of the fusion zone was obtained when the E312 electrode type was utilized to join both specimens.

Table 5 shows that electrode type (A), welding current (B), and welding speed (D) significantly affect the hardness test results. The factor that has the most significant influence is the type of electrode factor of 56.63%, followed by the welding speed factor of 14.65% and the current welding factor of 10.75%. Meanwhile, arc voltages (C) do not significantly affect hardness value.

Table 5. Analysis of variance for hardness.

Factor	DF	Seq. SS	Contribution	Adj. SS	Adj. MS	F-Value	F Table
A	2	12,539.5	56.63%	12,539.5	6269.8	34.30	3.55
B	2	2381.0	10.75%	2381.0	1190.5	6.51	3.55
C	2	689.3	3.11%	689.3	344.7	1.89	3.55
D	2	3243.5	14.65%	3243.5	1621.8	8.87	3.55
error	18	3290.1	14.86%	3290.1	182.8		
SS Total	26	22,143.4	100%				

DF = degrees of freedom; Seq. ss = Sequential sums of squares; Adj. SS = Adjusted sums of squares; Adj. MS = Adjusted mean squares.

3.2. Tensile Strength Results

Figure 4 shows tensile test samples of SS316 and low-carbon steel with nine parameter variations based on the L9 orthogonal array. Each sample of various parameters undergoes permanent deformation in the fracture area, indicating that all joint welding tends to be ductile. The tensile test results show the fracture area on the tensile test specimen in the HAZ of the low-carbon steel side. It is indicated that the metal in the fusion zone has a higher strength than the base metal.

A signal-to-noise (S/N) ratio analysis of tensile strength can be shown in Figure 5. The tensile strength decreases with the change in electrode type, although not significantly enough. Welding current increased the weld joint's tensile strength up to 100A and then reduced it. The tensile strength of the weld joint decreases up to 16 V and then increases by 18 V. The increasing welding speed leads to the decreased tensile strength of the weld joint. The highest yield of the tensile strength signal to noise (S/N) ratio based on the

larger-the-better could be attained at the combined settings of A1, B2, C1, and D1, i.e., an electrode type of E 308, a welding current of 100 A, an arc voltage of 14 V and a welding speed of 4 cm/min.



Figure 4. Tensile test samples of SS316 and low-carbon steel.

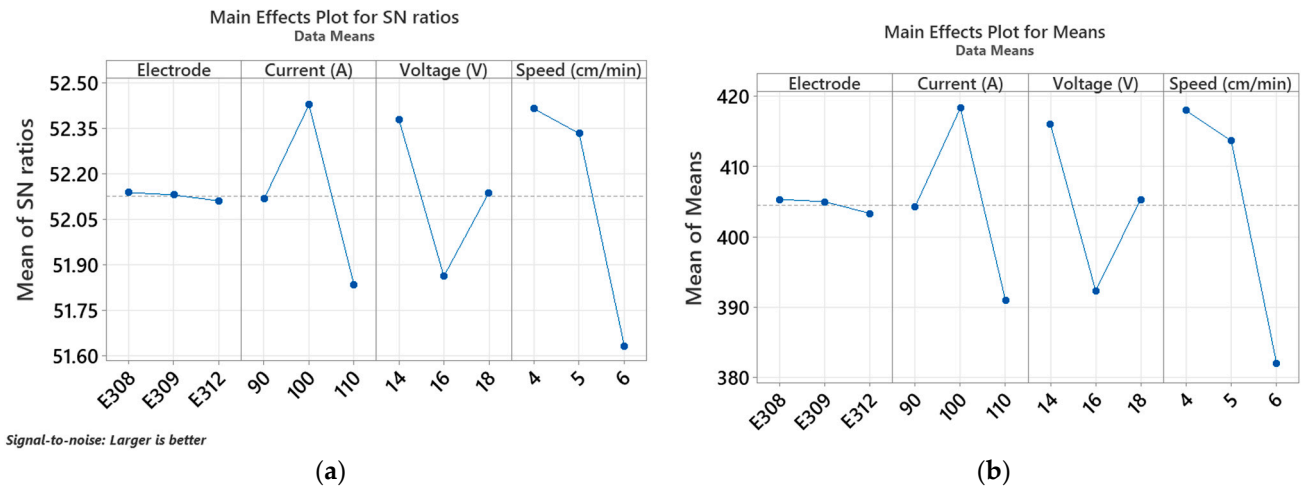


Figure 5. Response graphs of tensile strength against various factors; (a) Mean of S/N ratio and (b) Mean of Means.

The analysis of variance procedure was used to establish the relative significance of the factors as shown in Table 6. ANOVA is a table of information that displays the relative influences of factors and interactions assigned to the column of an orthogonal array. The ANOVA table shows that welding speed has the maximum significant contribution to determining the tensile strength of the welding joint (52.02%). On the other hand, the electrode type did not significantly contribute to determining the tensile strength of the welding joint. The type of electrode used during welding will affect the composition of the fusion zone. Deposited chemical composition has the effect of determining the resulting mechanical strength. However, in this experiment, the analysis of variance showed that the electrode type used did not make a significant contribution (0.16%) to the tensile strength of the weld joint. The E308 electrode provides maximum results in the tensile strength of the weld joint. A chemical reaction usually produces gases such as nitrogen, oxygen, and hydrogen during welding. They will interact with the molten metal and can affect the mechanical properties of the welded joint [1].

Table 6. The analysis of variance for tensile strength of SS316 and low-carbon steel weld joints.

Factor	DF	Seq. SS	Contribution	Adj. SS	Adj. MS	F-Value	F Table
A	2	20.70	0.16%	20.73	10.36	0.52	3.55
B	2	3415.70	26.16%	3415.69	1707.84	85.81	3.55
C	2	2469.10	18.91%	2469.11	1234.56	62.03	3.55
D	2	6790.90	52.02%	6790.87	3395.44	170.60	3.55
Error	18	358.30	2.74%	358.26	19.90		
SS Total	26	13,054.70	100.00%				

Welding current and arc voltage are closely related to the heat transferred from the heat source to the workpiece. Heat input determines the phase of transformation, resulting in the microstructural characteristics of the weld. Table 6 shows that welding current (26.16%) and arc voltage (18.91% C) significantly contribute to tensile strength.

The results of the ANOVA in Table 6 reveal that welding speed has the highest significant contribution (52.02%) on the tensile strength. The welding speed will affect the amount of heat input in the welding process. The heat input is essential in determining the face and root weld [26,27]. Furthermore, heat input also affects the heat-affected zone and affects grain formation. Chuaiphan et al. [28] reported that dendrite size in the fusion zone tends to be smaller at high welding speeds, and pitting corrosion potential increases on the weld metal.

3.3. Flexural Strength Results

The study of four parameters (electrode type, welding current, arc voltage, and welding speed) concerning the flexural strength, in terms of the main effects plot for means and main effects plot for S/N ratios for each interaction, is elucidated in Figure 6.

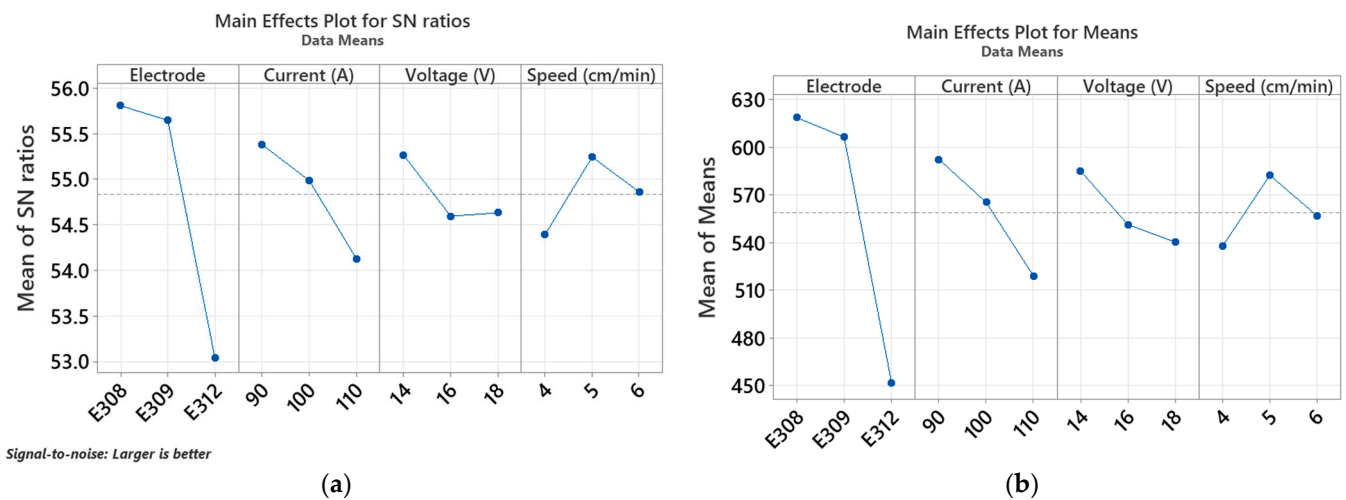


Figure 6. S/N ratio and mean response graphs for maximum flexural force; (a) Mean of S/N ratios and (b) Mean of Means.

Typical samples of flexural testing are presented in Figure 7. The flexural strength increased with the increasing welding current and arc voltage. Furthermore, the highest flexural strength was obtained at electrode type E312 and a welding speed of 5 cm/min. The larger-the-better flexural strength concerning the electrode type, welding current, arc voltage, and welding speed demonstrated the optimal input factor values (A1, B1, C1, and D2).

According to Table 7 and the analysis of variance for the flexural strength of SS316 and low-carbon steel weld joints, the electrode type factor has the most decisive influence,

accounting for 76.74 percent, followed by the welding current component, accounting for 12.20 percent.



Figure 7. Samples of flexural test.

Table 7. The analysis of variance for the flexural strength of SS316 and low-carbon steel weld joints.

Factor	DF	Seq. SS	Contribution	Adj. SS	Adj. MS	F-Value	F Table
A	2	155,183	76.74%	155,183	77,591.6	382.20	3.55
B	2	24,676	12.20%	24,676	12,338.2	60.78	3.55
C	2	9677	4.79%	9677	4838.5	23.83	3.55
D	2	9041	4.47%	9041	4520.4	22.27	3.55
Error	18	3654	1.81%	3654	203.0		
SS Total	26	202,232	100.00%				

The S/N ratio technique described above creates three sets of ideal input parameters for each of the three responses. Finding a single set of combined ideal settings for a variety of responses is crucial for real-world applications. Consequently, GRA is used in this study for multi-response optimization of the four components and three responses.

3.4. Multi-Response Optimization Using GRA

The practical application of GRA can solve problems with a limited amount of data. GRA generally uses grey assumptions, where the system’s behavior has uncertainty towards a black solution (i.e., there is not enough information data) or white only (i.e., the system has all the information).

The grey relational generation stage is carried out through experimental data on hardness, bend, and tensile strength responses, as shown in Table 4. Normalizing the data with Equation (4) yielded the reference sequence of responses ranging from 0 to 1. The deviation sequences were then computed using Equation (5). Table 8 shows the reference and deviation sequences produced following data pre-processing.

Using Equation (6), the GRC ($\xi_i(k)$) of each response was calculated, and the GRG (γ_i) was determined using the average GRC. As the results in Table 9 show, the calculation of S/N ratio of GRG values indicates whether they are suitable for further analysis. A higher S/N ratio value is favorable and indicates that the experimental data are close to the ideal normalized value of GRG [29].

Table 8. Reference and deviation sequences.

Run	Normalized Values (x_i^*)			Deviation Sequences (Δ_{0i})		
	Hardness	Tensile Strength	Flexural Strength	Hardness	Tensile Strength	Flexural Strength
1	0.1304	0.9524	1.0000	0.8696	0.0476	0.0000
2	0.0870	0.7302	0.9416	0.9130	0.2698	0.0584
3	0.0000	0.0159	0.6387	1.0000	0.9841	0.3613
4	0.0870	0.0000	0.9015	0.9130	1.0000	0.0985
5	0.8841	1.0000	0.6934	0.1159	0.0000	0.3066
6	0.7971	0.6667	0.8504	0.2029	0.3333	0.1496
7	0.6812	0.6825	0.3905	0.3188	0.3175	0.6095
8	0.7681	0.5714	0.3613	0.2319	0.4286	0.6387
9	1.0000	0.3333	0.0000	0.0000	0.6667	1.0000

Table 9. Grey relational grade (GRG) rank.

Run	Grey Relational Coefficient (ξ_i)			GRG (γ_i)	S/N Ratio of GRG	Rank
	Hardness	Tensile Strength	Flexural Strength			
1	0.3651	0.9130	1.0000	0.7594	-2.391	2
2	0.3538	0.6495	0.8954	0.6329	-3.973	5
3	0.3333	0.3369	0.5805	0.4169	-7.599	9
4	0.3538	0.3333	0.8354	0.5075	-5.891	8
5	0.8118	1.0000	0.6199	0.8106	-1.824	1
6	0.7113	0.6000	0.7697	0.6937	-3.177	3
7	0.6106	0.6117	0.4507	0.5576	-5.073	6
8	0.6832	0.5385	0.4391	0.5536	-5.136	7
9	1.0000	0.4286	0.3333	0.5873	-4.623	4

After the determination of the GRG rank, the GRG of each level factor was selected and averaged to produce the average GRG for the individual factor and assembled to create the response table shown in Table 10. The grades in the responses table represent the correlation between the reference sequence and the GRA comparability sequence. Higher GRG mean values imply a high association [30]. As a result of the GRG response table in Table 10, it is possible to arrive at the ideal parameter combination that maximizes total response.

Table 10. Response table of GRGs.

Level	Factors			
	A	B	C	D
Level 1	0.6031	0.6082	0.6689	0.7191
Level 2	0.6706	0.6657	0.5759	0.6281
Level 3	0.5662	0.5660	0.5950	0.4927
Delta	0.1044	0.0997	0.0930	0.2264
Rank	2	3	4	1

An ANOVA was run at a 95% confidence level for the grey relational grade to evaluate each component’s relevance and percentage contribution to the multiple performance parameters of dissimilar welding of SS316 and low-carbon steel. Considering the numerous reactions of hardness, tensile and flexural strength, Table 11 shows that the welding speed has the most significant influence on the GRG (57.21%), followed by the electrode type (11.71%), welding current (10.38%), and arc voltage (9.95%). Furthermore, because the F-values for all components are higher than F tables (3.55), it can be concluded that all factors substantially influence the dissimilar welding performance of SS316 and low-carbon steel.

Table 11. ANOVA for grey relational grade.

Factor	DF	Seq. SS	Contribution	Adj. MS	Adj. SS'	F-value	F-table
A	2	0.0505	11.71%	0.0252	0.0471	15.1378	3.55
B	2	0.0451	10.38%	0.0226	0.0418	13.5307	3.55
C	2	0.0434	9.95%	0.0217	0.0400	13.0133	3.55
D	2	0.2336	57.21%	0.1168	0.2303	70.0899	3.55
Error	18	0.0300	10.76%	0.0017	0.0433		
SS Total	26	0.4023	100%				

The current study shows that a welding speed as low as 4 cm/min delivers the highest contribution to the results. These results are in accordance with previous reports [1,31]. The welding speed parameter has significant influence in determining the total heat input per unit of weld length. Due to the slower speed, larger heat-affected zones are created, which increases the melting efficiency.

3.5. Prediction of Optimum Level

Confirmation of experiments for Taguchi analysis must be carried out to ensure that the results of Taguchi analysis are truly relevant or confirmed following the results of statistical calculations. In this experiment, test confirmation was carried out for the hardness test, tensile test, and bending test results.

The calculation of the optimum condition (OC) of the Taguchi approach is based on Equation (8).

$$OC = T + (A - T) + (B - T) + (C - T) + (D - T) \tag{8}$$

where *T* is the current grand average of performance. The confidence interval (CI) can be calculated by Equation (9).

$$CI = \pm \sqrt{F(1, n_e) * \frac{V_e}{N_e}} \tag{9}$$

where *F* (1, *n_e*) is the computed value of *F* at a desired confidence level with *n_e* being the error DOF, *V_e* being the error variance, and *N_e* being the effective number of replications.

Hardness testing is carried out on the fusion zone of the specimen. The larger-the-better hardness concerning electrode type, welding current, arc voltage, and welding speed presented the optimum values of input factor (A3 = 262, B3 = 247, C1 = 245 and D1 = 252) HBW, respectively, as shown in Table 12. Therefore, the hardness expected result in optimal conditions was 240 + (262 - 240) + (247 - 240) + (245 - 240) + (252 - 240) = 286 HBW.

Table 12. Resume of optimal welding parameters based on Taguchi's "larger is better".

No.	Properties	Parameters			
		Electrode Type (A)	Welding Current (B)	Arc Voltage (C)	Welding Speed (D)
1	Hardness	E312 (A3)	110 A (B3)	14V (C1)	4 cm/min (D1)
2	Tensile strength	E308 (A1)	100 A (B2)	14 V (C1)	4 cm/min (D1)
3	Flexural strength	E308 (A1)	90 A (B1)	14V (C1)	5 cm/min (D2)

The expected hardness on the fusion zone of the specimen at the optimum condition is 286. The 90% confidence interval (CI) for the expected yield from the confirmation experiment can be calculated using Equation (9), where *F*(1.18) = 4.41, *V_e* = 182.8, *N_e* = 3.86, and the confidence level = 90%. Therefore, the expected result at optimum condition = 286 ± 14.443 or 271.557 to 300.443 HBW. Following the previously disclosed calculating technique, the validation test of hardness, tensile, and flexural strength can be seen in Table 13.

Table 13. Result of validation tests of Taguchi’s approach.

No.	Properties	Experimental Results	Expected Results
1	Hardness (HBW)	272	271.557–300.443
2	Tensile strength (MPa)	408.91	426.546–459.654
3	Flexural strength (MPa)	684.96	682.726–717.274

Furthermore, grey based optimization offers a method to determine optimal parameters. The response of GRG, which is previously calculated as shown in Table 8, states the optimum level is A2, B2, C1, and D1. The final stage is to forecast the quality features using Equation (10) after determining the best value of the components using GRG.

$$\gamma_{predicted} = \gamma_m + \sum_{1=i}^q \gamma_o - \gamma_m \tag{10}$$

where o is the maximum of the average GRG at the optimum level of factors, and m is the mean GRG. The letter q represents the number of factors that influence response values. Table 14 further illustrates the expected values compared to the GRG initial experimental settings (Table 9). Furthermore, the GRG is improved by 23.0%. This improvement in GRA outcomes over the parameters in higher GRG values justifies the Taguchi approach used in conjunction with grey relational analysis to improve joining performance.

Table 14. Optimum GRG prediction.

Parameters	Initial GRG	Improved GRG Prediction
Setting level	A1 B1 C1 D1	A2 B2 C1 D1
Grey relational grade	0.7594	0.8844
Improvement in GRG		23.0%

3.6. Microstructure Evaluation

The microstructure of dissimilar welding can be predicted by constitution diagrams, e.g., the Schaeffler diagram. It estimates weldability and phase formation in the fusion zone using different electrodes [32]. Schaeffler diagrams can predict the proportions of martensite, austenite, and ferrite, as shown in Figure 8.

The chromium equivalent is calculated from the weight percentage of ferrite-forming elements (Cr, Si, Mo, Nb, W). The nickel equivalent is calculated from the weight percentage of austenite-forming elements (Ni, Co, Mn, Cu, N, C). Cr and Ni equivalents were obtained using the following expressions:

$$Cr_{eq.} = (Cr) + 2(Si) + 1.5(Mo) + 5(V) + 5.5(Al) + 1.75(Nb) + 1.5(Ti) + 0.75(W) \tag{11}$$

$$Ni_{eq.} = (Ni) + (Co) + 0.5(Mn) + 0.3(Cu) + 25(N) + 30(C) \tag{12}$$

All concentrations are represented as a percentage of total weight. The Schaeffler diagram is an essential tool for estimating the composition of austenitic Cr-Ni steel welds with carbon concentrations as low as 0.12%.

Figure 8a shows the macrostructure of the weld using E308. In this welding condition, the dilution ratio is about 15%. According to the Schaeffler diagram and corresponding dilution ratios, it exhibits a ferrite–austenite–martensite microstructure. The hardness test results in Table 4 show that welding using the E308 electrode produces the lowest hardness, indicating a small amount of martensitic phase.

According to the Schaeffler diagram, using the E309 electrode type for joining carbon steel and SS316 exhibits austenite–ferrite microstructure, as seen in Figure 8b. The fusion zone with an austenite microstructure in this condition tends to be prone to hot cracking. Low-melting eutectics, such as S and P, and alloy elements, such as Ti and Nb produce

hot cracking in stainless steel welds [33]. Application of the E312 electrode for joining the carbon steel and stainless steel is predicted to prompt embrittlement when heat treatment or high-temperature service is applied. The appearance of the phase in the fusion zone is predicted by the Schaeffler diagram, as shown in Figure 8c.

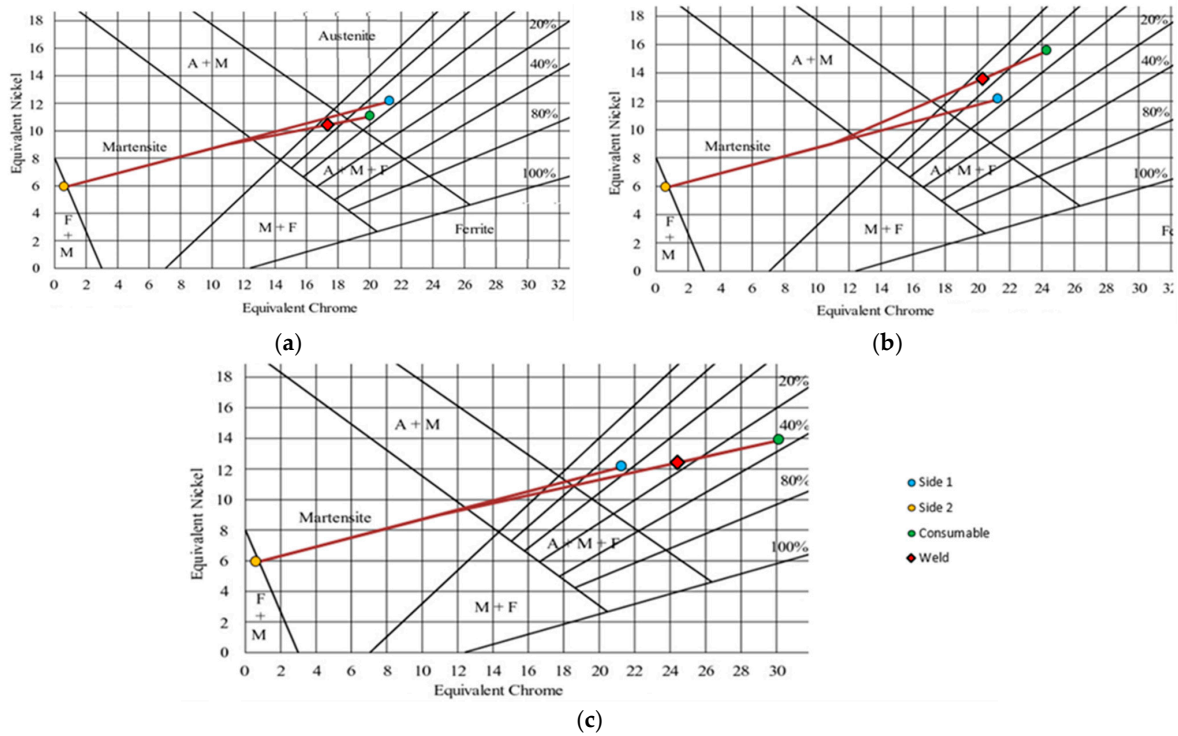


Figure 8. Predicted fusion zone microstructure of dissimilar carbon steel and SS316 weld using a Schaeffler diagram in (a) E308 welding electrode, (b) E309 welding electrode, (c) E312 welding electrode.

Figure 9 shows the fusion zone of the welded joint using the E308 electrode type. It can be seen that austenite and ferrite phases formed. The austenite phase is more dominant than the other phases, with a face-centered cubic (FCC) structure. The austenite phase has an essential role in determining the ductility properties. Furthermore, increasing ductility can prolong failure time under the influence of external loads and stress.



Figure 9. Fusion zone of the weld joint with the E308 electrode type.

4. Summary

The Taguchi method optimized the optimum parameter conditions of the dissimilar weld between SS316 and ASTM A36 via the shielded metal arc welding method. An L9 orthogonal array was used to accommodate the experiment. An ANOVA showed that all four welding parameters, electrode type, welding current, arc voltage, and welding speed, significantly affected the hardness and tensile and flexural strength. The following simultaneous optimal condition parameters were obtained through GRA-based analysis: A2, B2, C1, and D1, corresponding to electrode type E309, a welding current of 100A, an arc voltage of 14V, and a welding speed of 4 cm/min, which predicted a performance improvement of 23.0%.

Author Contributions: Conceptualization, D.K.P. and A.A.; methodology, D.K.P. and A.A.; software, G., A. and A.M.; validation, A.A., G. and A.; formal analysis, D.K.P., and A.M.; investigation, A.; resources, D.K.P.; data curation, A.; writing—original draft preparation, A.; writing—review and editing, A.A. and G.; visualization, G.; supervision, D.K.P.; project administration, A.M.; funding acquisition, D.K.P. All authors have read and agreed to the published version of the manuscript.

Funding: This research received no external funding.

Acknowledgments: The authors are grateful to Sriwijaya University for supporting and providing the facilities for this research.

Conflicts of Interest: The authors declare no conflict of interest.

References

1. Kuo, S. *Welding Metallurgy*; John Wiley & Sons, Inc.: Hoboken, NJ, USA, 2002.
2. Phillips, D.H. *Welding Engineering: An Introduction*; Wiley: Hoboken, NJ, USA, 2016.
3. Mohammed, R.; Reddy, G.M.; Rao, K.S. Studies on microstructure, mechanical and corrosion properties of high nitrogen stainless steel shielded metal arc welds. *IOP Conf. Ser. Mater. Sci. Eng.* **2018**, *330*, 012044. [[CrossRef](#)]
4. Dak, G.; Pandey, C. A critical review on dissimilar welds joint between martensitic and austenitic steel for power plant application. *J. Manuf. Process.* **2020**, *58*, 377–406. [[CrossRef](#)]
5. Gunawan, G.; Arifin, A. Intergranular Corrosion and Ductile-Brittle Transition Behaviour in Martensitic Stainless Steel. *Indones. J. Eng. Sci.* **2021**, *2*, 31–41. [[CrossRef](#)]
6. Jula, M.; Dehmlaei, R.; Zaree, S.R.A. The comparative evaluation of AISI 316/A387-Gr.91 steels dissimilar weld metal produced by CCGTAW and PCGTAW processes. *J. Manuf. Process.* **2018**, *36*, 272–280. [[CrossRef](#)]
7. Kulkarni, A.; Dwivedi, D.; Vasudevan, M. Microstructure and mechanical properties of A-TIG welded AISI 316L SS-Alloy 800 dissimilar metal joint. *Mater. Sci. Eng. A* **2020**, *790*, 139685. [[CrossRef](#)]
8. Bright, O.; Ming, H.; Wang, J.; Meng, F.; Xu, S.; Han, E.-H. Microstructural Characterization of Low Alloy Steel A508–309/308L Stainless Steel Dissimilar Weld Metals. *Int. J. Press. Vessel. Pip.* **2021**, *190*, 104297.
9. Fang, Y.; Jiang, X.; Mo, D.; Zhu, D.; Luo, Z. A review on dissimilar metals' welding methods and mechanisms with interlayer. *Int. J. Adv. Manuf. Technol.* **2019**, *102*, 2845–2863. [[CrossRef](#)]
10. Khan, W.N.; Chhibber, R. Effect of filler metal on solidification, microstructure and mechanical properties of dissimilar super duplex/pipeline steel GTA weld. *Mater. Sci. Eng. A* **2020**, *803*, 140476. [[CrossRef](#)]
11. Khamari, B.K.; Dash, S.S.; Karak, S.K.; Biswal, B.B. Effect of welding parameters on mechanical and microstructural properties of GMAW and SMAW mild steel joints. *Ironmak. Steelmak.* **2019**, *47*, 844–851. [[CrossRef](#)]
12. Singh, D.K.; Sahoo, G.; Basu, R.; Sharma, V.; Mohtadi-Bonab, M. Investigation on the microstructure—Mechanical property correlation in dissimilar steel welds of stainless steel SS 304 and medium carbon steel EN 8. *J. Manuf. Process.* **2018**, *36*, 281–292. [[CrossRef](#)]
13. Manikandan, M.; Gunachandran, R.; Vigneshwaran, M.; Sudhakar, S.; Srikanth, A.; Venkateshkannan, M.; Arivarasu, M.; Arivazhagan, N.; Rajan, D.N. Comparative Studies on Metallurgical and Mechanical Properties of Bimetallic Combination on Incoloy 800 and SS 316L Fabricated by Gas Metal and Shield Metal Arc Welding. *Trans. Indian Inst. Met.* **2017**, *70*, 749–757. [[CrossRef](#)]
14. Verma, J.; Taiwade, R.V. Dissimilar welding behavior of 22% Cr series stainless steel with 316L and its corrosion resistance in modified aggressive environment. *J. Manuf. Process.* **2016**, *24*, 1–10. [[CrossRef](#)]
15. Verma, J.; Taiwade, R.V.; Khatirkar, R.K.; Kumar, A. A Comparative Study on the Effect of Electrode on Microstructure and Mechanical Properties of Dissimilar Welds of 2205 Austeno-Ferritic and 316L Austenitic Stainless Steel. *Mater. Trans.* **2016**, *57*, 494–500. [[CrossRef](#)]
16. Ghosh, N.; Pal, P.K.; Nandi, G. GMAW dissimilar welding of AISI 409 ferritic stainless steel to AISI 316L austenitic stainless steel by using AISI 308 filler wire. *Eng. Sci. Technol. Int. J.* **2017**, *20*, 1334–1341. [[CrossRef](#)]

17. Daniyan, I.A.; Mpofu, K.; Adeodu, A.O. Optimization of welding parameters using Taguchi and response surface methodology for rail car bracket assembly. *Int. J. Adv. Manuf. Technol.* **2018**, *100*, 2221–2228. [[CrossRef](#)]
18. Mahmood, N.Y.; Alwan, A.H. Mechanical properties improvement of MIG welding steel sheets using Taguchi method. *Aust. J. Mech. Eng.* **2019**, *20*, 66–73. [[CrossRef](#)]
19. Taguchi, G.; Chowdhury, S.; Wu, Y. *Taguchi's Quality Engineering Handbook*; John Wiley & Sons, Inc.: Hoboken, NJ, USA, 2004.
20. Oemar, B.; Chang, W.-C. Taguchi method for optimizing process parameters in the production of activated carbon from rubber seed shell. *Int. J. Adv. Manuf. Technol.* **2020**, *107*, 4609–4620. [[CrossRef](#)]
21. Arifin, A.; Gunawan, G.; Yani, I.; Yanis, M.; Pradifita, R. Optimization of Stir Casting Method of Aluminum Matrix Composite (AMC) for the Hardness Properties by Using Taguchi Method. *J. Kejuruter.* **2017**, *29*, 35–39. [[CrossRef](#)]
22. Kanchana, J.; Prasath, V.; Krishnaraj, V.; Geetha Priyadharshini, B. Multi response optimization of process parameters using grey relational analysis for milling of hardened Custom 465 steel. *Procedia Manuf.* **2019**, *30*, 451–458. [[CrossRef](#)]
23. Manoharan, S.; Krishnaraj, V.; Vijay, R.; Singaravelu, D.L.; Suresha, B. Development and characterization of novel fiber reinforced hybrid friction composites. In *Green Composites*; Davim, J.P., Ed.; De Gruyter: Berlin, Germany; Boston, MA, USA, 2017; pp. 69–114.
24. Gomes, A.J.C.; Jorge, J.C.F.; Bott, I.S.; Souza, L.F.G.; Mendes, M.C.; Araújo, L.S. Influence of Chemical Composition on the Mechanical and Microstructural Properties of High Strength Steel Weld Metals Submitted to PWHT. *Met. Microstruct. Anal.* **2019**, *8*, 815–825. [[CrossRef](#)]
25. Pouranvari, M.; Marashi, S.P.H. Dissimilar Spot Welds of Aisi 304/Aisi 1008: Metallurgical and Mechanical Characterization. *Steel Res. Int.* **2011**, *82*, 1355–1361. [[CrossRef](#)]
26. Choudhary, A.; Kumar, M.; Unune, D.R. Experimental investigation and optimization of weld bead characteristics during submerged arc welding of AISI 1023 steel. *Def. Technol.* **2018**, *15*, 72–82. [[CrossRef](#)]
27. Kannan, T.; Yoganandh, J. Effect of process parameters on clad bead geometry and its shape relationships of stainless steel claddings deposited by GMAW. *Int. J. Adv. Manuf. Technol.* **2009**, *47*, 1083–1095. [[CrossRef](#)]
28. Chuaiphan, W.; Srijaroenpramong, L. Effect of welding speed on microstructures, mechanical properties and corrosion behavior of GTA-welded AISI 201 stainless steel sheets. *J. Mater. Process. Technol.* **2014**, *214*, 402–408. [[CrossRef](#)]
29. Lyu, Y.; Wahlström, J.; Tu, M.; Olofsson, U. A Friction, Wear and Emission Tribometer Study of Non-Asbestos Organic Pins Sliding Against AlSiC MMC Discs. *Tribol. Ind.* **2018**, *40*, 274–282. [[CrossRef](#)]
30. Kasemsiri, P.; Dulsang, N.; Pongsa, U.; Hiziroglu, S.; Chindaprasirt, P. Optimization of Biodegradable Foam Composites from Cassava Starch, Oil Palm Fiber, Chitosan and Palm Oil Using Taguchi Method and Grey Relational Analysis. *J. Polym. Environ.* **2016**, *25*, 378–390. [[CrossRef](#)]
31. Cao, L.; Shao, X.; Jiang, P.; Zhou, Q.; Rong, Y.; Geng, S.; Mi, G. Effects of Welding Speed on Microstructure and Mechanical Property of Fiber Laser Welded Dissimilar Butt Joints between AISI316L and EH36. *Metals* **2017**, *7*, 270. [[CrossRef](#)]
32. Brandi, S.D.; Schon, C.G. A Thermodynamic Study of a Constitutional Diagram for Duplex Stainless Steels. *J. Phase Equilibria Diffus.* **2017**, *38*, 268–275. [[CrossRef](#)]
33. Shankar, V.; Gill, T.P.S.; Mannan, S.L.; Sundaresan, S. Solidification cracking in austenitic stainless steel welds. *Sadhana* **2003**, *28*, 359–382. [[CrossRef](#)]

Disclaimer/Publisher's Note: The statements, opinions and data contained in all publications are solely those of the individual author(s) and contributor(s) and not of MDPI and/or the editor(s). MDPI and/or the editor(s) disclaim responsibility for any injury to people or property resulting from any ideas, methods, instructions or products referred to in the content.